AUT Journal of Electrical Engineering
10.22060/EEJ.2026.26568.6160

Machine-Learning-Assisted Inverse Design of an Artificial-Magnetic-Conductor-Backed Antenna for Wearable and Internet-of-Things Applications†

Nishant Kumar*[1], Rashmi Sinha[1]
[1]Department of Electronics and Communication Engineering, NIT Jamshedpur, Jamshedpur 831014, Jharkhand, India
*Corresponding author
E-mail address: 2023rsec009@nitjsr.ac.in

Abstract

The relationship between the geometric parameters and electromagnetic responses of artificial magnetic conductor (AMC) backed wearable antennas is very nonlinear in nature. However, the conventional full-wave optimization requires a long computation time particularly for the simultaneous optimization of the antenna parameters and AMC parameters. A data-driven machine-learning approach for an AMC-backed wearable antenna is proposed along with graphical user interfaces (GUIs) for an automatic processing of the electromagnetic data and very fast geometry prediction.First, a small size meander-line monopole antenna and a periodic AMC unit cell are designed and analyzed based on the electromagnetic theory and CST Microwave Studio simulation. All 654 antenna configurations are generated by the parametric sweeps in a frequency band of 2.0-6.0 GHz. The eight supervised-learning models are comparatively evaluated by using mean absolute error (MAE), root mean square error (RMSE) and coefficient of determination (R^2); where the support vector regressor (SVR) achieved the best results with a MAE of 0.00519 GHz and R^2 of 0.9998 in the prediction of resonance frequency and minimum S_{11} of 0.248 dB and 0.9441, respectively.The proposed framework performs an inverse design by finding the geometry of the antenna that can achieve the desired resonance frequency and matching condition, and an inverse multilayer perceptron is used to predict the AMC-unit-cell geometries with desired 0° reflection-phase crossing, which is then verified in CST. The coupled antenna–AMC configuration, a gain improvement from 1.16 to 4.46 dBi and a decrease in peak 1-g SAR from 34.3 to 1.23 W/kg are obtained.

Keywords:

wearable antenna; artificial magnetic conductor; inverse design; machine learning; specific absorption rate.

1. Introduction

Wearable antennas are being widely used in healthcare monitoring systems, smart textiles, wireless sensing, military communication systems and Internet-of-Things (IoT) systems and hence an indispensable part of the body-area network (BAN) systems [1-5]. A wearable antenna is situated in a reactive near field of a biological tissue having high relative permittivity and finite conductivity that loads the antenna and influences its input impedance, resonant frequency, radiation pattern and total efficiency. The same is true of the proximity, about the part radiated energy that is absorbed by tissues. This absorption is measured by the specific absorption rate (SAR) which is regulated by the FCC at an average of 1.6 W/kg per gram of tissue and by ICNIRP at an average of 2 W/kg per 10 grams of tissue. There are several conflicting requirements that must be taken into account when designing a practical wearable antenna – compact and low-profile geometry, low SAR, forward radiation and body loading tolerant impedance matching.

An artificial magnetic conductor (AMC) (also known as a high impedance surface) [1-13] is one of the most promising structures. A conventional perfect electric conductor (PEC) reflects a wave normally incident on it, with phase shift of ~180° and can never be placed in the vicinity of a radiator without destroying the direct field. On the other hand, for an AMC, the phase of the reflection phase passes through 0° around the desired operation frequency, and reflected and direct fields are in phase even for small distances between the AMC and the antenna. This positioning of the AMC between the radiator and the body then leads to an enhanced realized gain, a higher front to back ratio, elimination of tissue loading effect on the radiator and finally the attenuation of radiation towards the body which in turn reduces the SAR.Recent studies have consistently demonstrated that wearable antennas with AMC backing show enhanced performance: gain enhancement of ~1.4-5.3 dB, higher Front to Back (F/B) ratio and SAR reduction of ~99% have been reported for textile, Substrate-integrated-waveguide (SIW), array, Multi-input-Multi-Output (MIMO) and multiband antennas backed by AMC [1-8] and breathable [9], flexible [10] and multilayer AMC [11] designs have also been reported.This work leads to two observations. The first is the electromagnetic advantage of AMC backing, is well documented, repeatable and can be used on different substrates, bands, radiator topologies. Second, these studies are all developed sequentially, with each one being tuned sequentially, from the radiator to a sweep of the AMC near the zero crossing of the AMC, and then sweeping the separation of the radiator (full wave simulation is repeated many times over). With the number of full-wave evaluations

† During the preparation of this work, the authors used ChatGPT (OpenAI) to improve language and readability. After using this tool, the authors reviewed and edited the content as needed and take full responsibility for the content of the publication.

Uncorrected Proof

increasing polynomially with the number of the geometric variables, the full-wave evaluation will become the major cost of the design cycle.

Moreover, when the AMC is combined with the antenna, if there is any mismatch in the resonance frequencies of the antenna and AMC, the gain of the surface is reduced. A few studies thus have tried to alleviate this burden of simulation using machine learning (ML): ensemble, decision-tree, random-forest, and Support Vector Regression (SVR) surrogates have been trained with full-wave data to predict antenna responses with a coefficient of deteremination (R^2) of approximately 0.88–0.98 [14-17] and reduced design time by 70–80% [14-16]; a comprehensive review is provided in [18].Other works predict geometry rather than the response [19-21] but typically for canonical patches for which there exist closed-form design equations, and nine regressors were compared for the design of a quasi-Yagi antenna in [22] and a physics-aware generative adversarial network (GAN) was used to design sparse arrays in [23]. Forward and inverse design of metasurfaces, which is intrinsically ill-posed [24,25] has also been investigated by deep learning, as well as the prediction of SAR hot-spots [26].The literature reviewed shows that there are four gaps. For the most part, most of the ML studies involving wearable antennas develop forward surrogates, and not the design problem of finding a geometry to yield a desired response. Second, the concept of inverse prediction is usually applied to canonical structures where analytical design equations exist, and the coupled antenna–AMC problem has not been thought of as a single inverse-design problem. Third, it is not always said that the inverse mapping is non-unique: there is no single scalar target to uniquely identify three (or more) geometric targets, so it is not an exact predictor, but an initializer, to be followed by full-wave verification. Fourth, reported pipelines are seldom automated, and reuse of pipelines with other designs is hard.

In this work, an inverse design technique to coordinate the design of the compact meander line wearable antenna and AMC backing is developed using machine learning. This proposed approach is a complementary approach to the full-wave electromagenetic interpretation and is termed as data-driven surrogate modeling. The meander-line antenna is analyzed by parametric simulation by using CST Microwave Studio to determine the relationship between the main geometric parameters of the antenna and the response of the antenna. Some models of supervised learning are then compared in terms of forward prediction and the best model is subsequently applied to the fast antenna inverse searching. A geometry-initialization model is built based on machine learning (ML) to find the candidate AMC unit-cell dimensions for a given zero-reflection-phase (ZRP) frequency. The antenna and AMC candidates are then combined together and the combined configuration is then analysed by full wave CST simulation.

The novelty of this work is the design method, but not a new radiator: both the antenna geometry and the AMC geometry are designed using ML based inverse design, and aligned before a single coupled full-wave verification, while the AMC-backed antennas in [1-11] were tuned by sequential parametric sweeping and the ML-assisted wearable antennas in [14-16] were based on ML as a forward surrogate. Moreover, the non-uniqueness of the AMC inverse mapping is quantified, the surrogates are tested with repeated and geometry-blocked data splits and the workflow is automated in two Graphical user interfaces (GUIs). The results are compared with previous studies in Table 12.

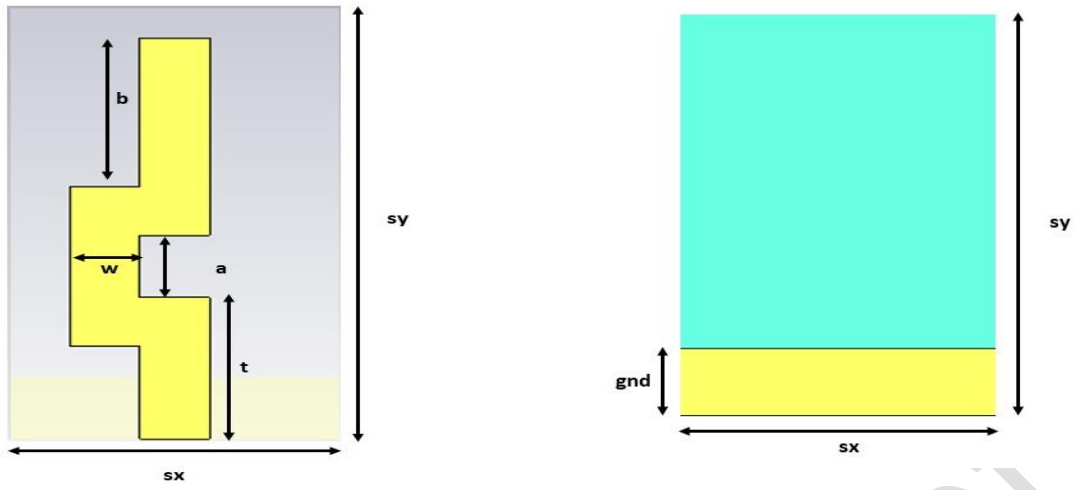
2. Antenna Design and Electromagnetic Modeling

2-1- Geometry and Structural Configuration

A compact printed meander-line monopole antenna is designed on an FR-4 substrate with the relative permittivity (ε_r) of about 4.3, a loss tangent of 0.02 and the substrate thickness (h) of 1.6 mm and is used as the reference antenna. The overall size of the substrate is 19 mm x 40 mm. A microstrip feed is used to excite the radiator and there is a truncated ground plane on the opposite side of the substrate, close to the feed area. The width of the meandered conducting strip is set to 4 mm, and the remaining geometric parameters, which are considered in the parametric study, are the meander sizes a and b. All the other geometrical, material and excitation parameters are held constant during CST simulations. The proposed geometry of the antenna is represented in the top and bottom views in Fig. 1. The summary of the corresponding reference dimensions of the antenna model are presented in Table 1. The dimensions a and b are then swept over the range of values and the remaining dimensions are kept at the set values.

Unconfirmed Proof

10.22060/EEJ.2026.26568.6160



(a) (b)

Fig.1. Proposed meander-line antenna: (a) front view , (b) back view

Table 1. Physical Dimensions of the Meander-Line Antenna.

Param.	Value (mm)	Description	Param.	Value (mm)	Description
s_x	19	Substrate width	*gndy*	5	Ground plane length
s_y	40	Substrate height	*t*	7.5	Feed gap
w	4	Trace width	*th*	0.035	Metal thickness
a	4.6	Middle meander segment length.	*b*	10.0	Upper meander segment length

The values given in Table 1 are the reference conditions of the antenna configuration for the standalone electromagnetic characterization. The inverse-designed geometry acquired by the consequent inverse-design process is reported in Section 6.4.

2-2- Resonance Condition and Electromagnetic Modeling

The monopole resonates at the first order, and it is largely dependent on the effective guided electrical length of the meander-line. A simplified quarter-wavelength relationship is given by

$$L_{\text{eff}} \approx \frac{\lambda_g}{4} = \frac{c}{4 f_r \sqrt{\varepsilon_{\text{eff}}}} \quad (1)$$

Its derivation is similar to that of the guided wavelength, except for the different form of the permittivity (ε_eff) and the inclusion of the effective current-path length (L_eff). The actual length of the antenna (path length) is less than the length of the corresponding straight monopole at the same frequency due to the fold.

The effective path length is $L_eff \approx N_v a + N_h b$, where N_v and N_h are the numbers of vertical and horizontal segments for a simplified meander geometry , this is interpretation of the current path rather than a closed form model.

The simulated reflection coefficient $\Gamma = (Z_{in} - Z_o)/(Z_{in} + Z_o)$, where Z_{in} is the input impedance of the antenna and $Z_o = 50\ \Omega$, is shown in dB as $S_{11}(f)$. The resonant frequency reduction in the meander structure is achieved by two main mechanisms: the first is due to the increase in the current path length, and the second is due to capacitive coupling between neighbouring parallel components. The effects of these can be understood on the basis of an equivalent RLC model, the approximate resonance of which is

Uncorrected Proof

10.22060/EEJ.2026.26568.6160

$$f_r \approx \frac{1}{2\pi\sqrt{LC}} \quad (2)$$

L and C are the effective inductive and capacitive loading of the meander structure. The simulated trends are explained here using the equivalent-circuit relation, and not used as an alternative to the CST results.

2-3- Parametric Analysis of the Antenna

The two main dimensions a and b of the meander are swept over a range of values as defined in Table 3 by a structured sweep. The simulated S_{11} of each geometry is analyzed to find the resonant frequency, minimum reflection coefficient and the impedance bandwidth. The parametric sweep file contains 654 unique antenna configurations for further machine learning analysis.

The resulting resonant-frequency surface exhibits a nonlinear but continuous frequency response of the antenna with the meander geometry as shown in Fig. 2. Generally, the longer the effective current-path, the lower the resonance frequency. The effect of each parameter may not be the same due to the mutual capacitance, current distribution and feed coupling changes in the meander sections. Hence, the CST sweep is kept as reference data set for model development and the effective-length and equivalent-RLC interpretations are employed to elucidate the observed trends [1].

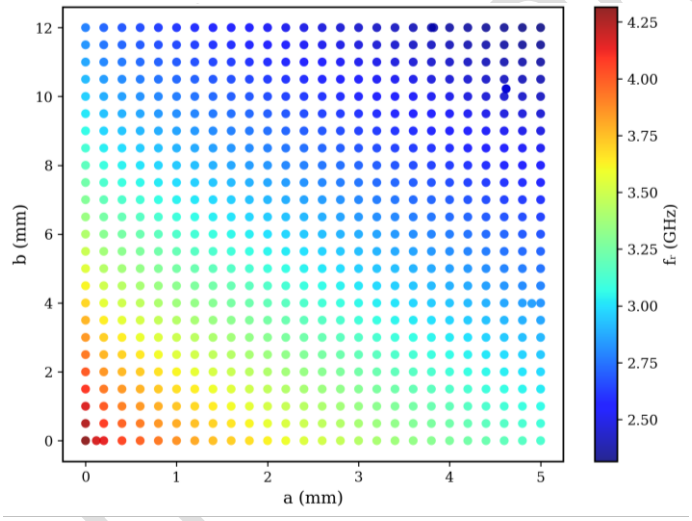
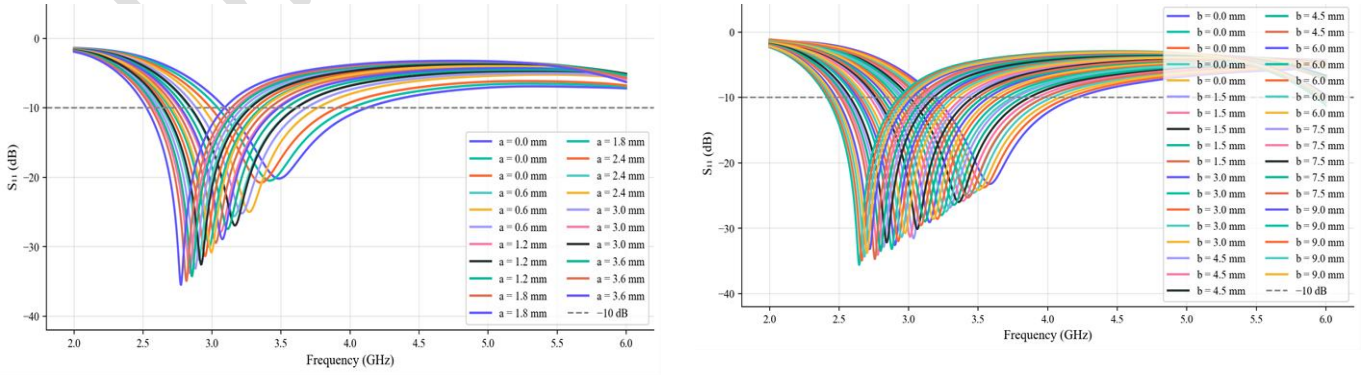


Fig. 2. Resonant-frequency design space of the meander-line antenna over the (a, b) parameter domain, interpolated from the 654 CST samples.

The individual effects of the swept parameters are determined by fixing the other parameter in the middle of its range. The S_{11} curves corresponding to the above are shown in Fig. 3. The resonance shift and the matching variation due to variation of the meander dimension are illustrated on these plots. They also give an indication of the quality of the design variables being used for predicting the antenna response: a check that would be valuable for the selected design variables to contain enough information.



(a) (b)

10.22060/EEJ.2026.26568.6160

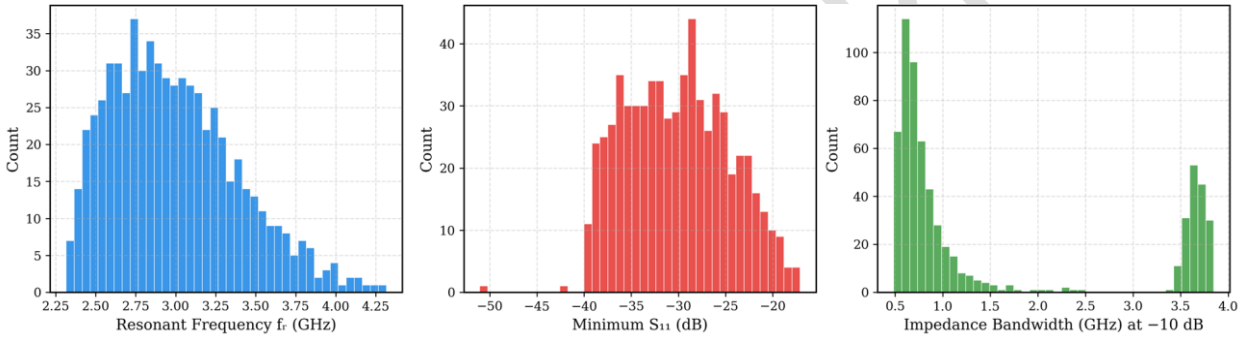
Fig. 3. Parametric S_{11} responses of the meander-line monopole: (a) variation of a with b fixed at its median value (6.0 mm); (b) variation of b with a fixed at its median value (2.6 mm).

2-4- Antenna Dataset and Statistical Characteristics

The CST parametric sweep gives rise to the database of electromagnetic fields to be used in the following machine-learning analysis. The simulated S_{11} response is computed across the frequency range 2–6 GHz (1001 points) for each unique antenna geometry and the principal scalar responses f_r, S_{11},min and the −10 dB impedance bandwidth are obtained. The entire $S_{11}(f)$ response is also stored for the entire-spectrum surrogate analysis described later in the paper. The antenna simulations use time domain solver,a Hexahedral Finite Intergration Technique (FIT) mesh , open boundary conditions and a waveguide port.

The antenna dataset, after removing duplications, has 654 unique geometrical configurations. Three runs of the sweep file were simulated with s_γ = 32 mm instead of 40 mm; one of them repeats the geometry (a, b) = (4.6212, 10.2228) mm and is removed as a duplicate, so two of the 654 samples, (a, b) = (4.9031, 3.9864) and (0.1187, 0) mm, have s_γ = 32 mm. Their effect on the accuracy is reported in Section 6.1. The extracted resonant frequencies range between 2.316-4.316 GHz, and the minimum S_{11} values are between −17 and −51 dB. The −10 dB impedance bandwidth of the band that contains the resonance ranges from 404 to 2440 MHz (median 638 MHz; the four largest values, for a = 0 and b ≤ 1.5 mm, are cut off at the 6 GHz edge of the simulation) across the geometry space investigated indicating that a change in the meander dimensions also alters the impedance matching and bandwidth.

The distribution of the electromagnetic response extracted is displayed in Fig. 4. The relatively wide envelope of the resonant-frequency and matching responses offer a good basis for training and testing surrogate models in the design space being considered.



(a) (b) (c)

Fig. 4. Dataset distributions: (a) resonant frequency f_r, (b) minimum S_{11}, (c) −10 dB bandwidth.

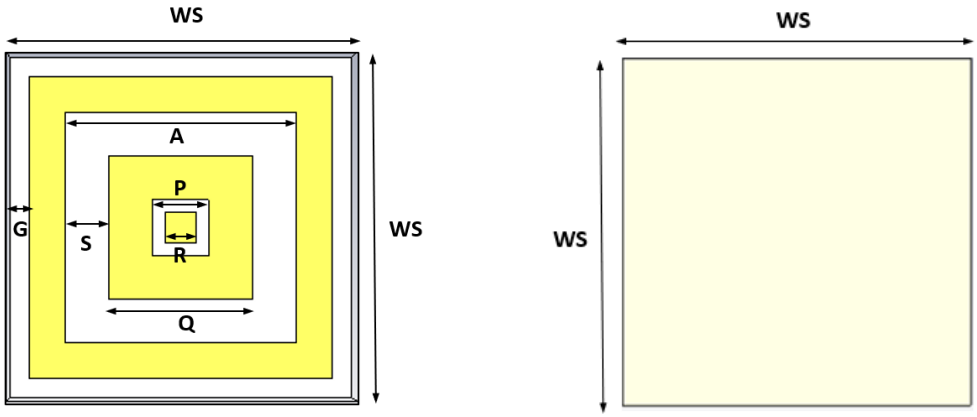
The generated antenna dataset in this section is used as a reference for the machine-learning methodology presented in Section 4. The AMC dataset is independently generated, and presented with the AMC unit-cell design in Section 3. At the inverse-design and coupled-electromagnetic-validation steps the two datasets are then merged.

3. AMC Unit-Cell Design and Reflection-Phase Modeling

3-1- Geometry and Configuration

The proposed AMC unit cell is a patterned metallic surface and integrated slots are printed on an FR-4 dielectric substrate. The relative permittivity of the substrate is ε_r = 4.3 and the thickness of the substrate is h=1.6 mm. The other side of the substrate is covered with a continuous metallic ground plane. WS = 22 mm is the fixed periodicity of the unit-cell. The three most important geometrical variables taken into consideration in the AMC design are patch width A, slot width S and the inter-slot gap G. The selection of these three parameters is chosen to directly change the surface-current path, capacitive coupling and electromagnetic interaction between adjacent parts of the patterned conductor. During the AMC parametric study, the other dimensions and material properties remain constant. The AMC unit-cell geometry is shown in the top and back views, respectively, in Fig. 5. Table 2 shows the reference AMC configuration's main dimensions.

Uncorrected Proof



(a) (b)

Fig. 5. AMC unit cell: (a) top view — patch and slot pattern, (b) back view.

Table 2. AMC Unit-Cell Dimensions.

Param.	Value (mm)	Description	Param.	Value (mm)	Description
WS	22	Unit-cell periodicity	h	1.6	Substrate thickness
A	14.888	Patch width	S	2.818	Slot width
G	1.207	Inter-slot gap	P = A−4S	3.617	Remaining patch width
Q = A−2S	9.253	Inner patch dim	R = 6S−A	2.019	Slot edge distance

3-2- Reflection Phase and Equivalent Surface-Impedance Interpretation

An equivalent surface impedance can be used to interpret the reflection-phase behaviour of the AMC. For a normally incident plane wave, the reflection coefficient of the AMC is $\Gamma_AMC = (Z_s - \eta_0)/(Z_s + \eta_0)$, where Z_s is the frequency-dependent surface impedance of the AMC and $\eta_0 \approx 377\ \Omega$ is the free-space impedance. At the AMC resonance, the amplitude of the surface impedance tends to increase making $\Gamma_AMC \sim +1$. As a result, the reflection phase tends towards 0° (in-phase reflection).

The response can be modelled as a parallel LC model, with a good approximation. One of the more popular forms for the equivalent surface impedance is

$$Z_s(\omega) \approx \frac{j\omega L}{1-\omega^2 LC} \qquad f_0 \approx \frac{1}{2\pi\sqrt{LC}} \tag{3}$$

where the effective inductance and capacitance added in by the surface current path and the spaces between the adjacent metallic areas are represented by L and C. The larger the width A the longer the surface current path and the greater the inductive and capacitive loading, causing f_0 to go down. If the width of this slot S is reduced generally the capacitive loading is reduced and the resonance frequency shifted to higher values. The lower the gap between the slots (G), the stronger the electromagnetic coupling between the neighboring sections and the lower the frequency of f_0 in general. These trends are used as physical checks of the CST results and predictions of the inverse model [1-3]. The reflection phase of the reference AMC unit cell is simulated as a function of frequency and is plotted in Fig. 6. A zero degree crossing is located near the intended operating region which will be used as the main AMC design target to be used in the subsequent inverse-design analysis.

Uncorrected Proof

10.22060/EEJ.2026.26568.6160

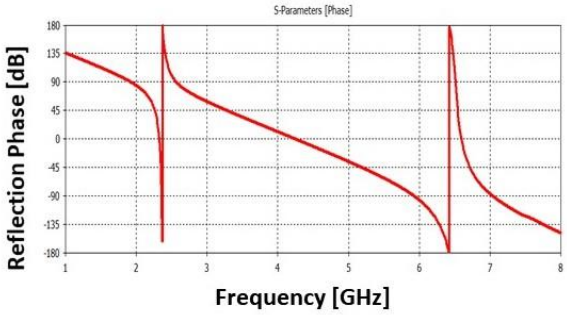
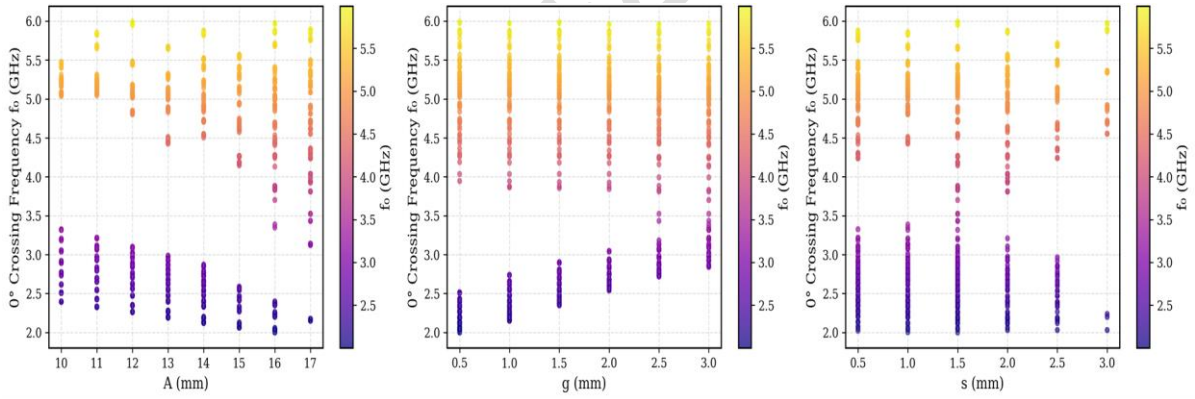


Fig. 6. Reflection phase of the AMC unit cell as a function of frequency.

3-3- Parametric Reflection-Phase Analysis

A structured parametric study is performed to study the effect of the AMC geometric variables. A, G and S are varied together on a grid (A: 10-17 mm in 1 mm increments; G, S: 0.5-3.0 mm in 0.5 mm increments) while the other parameters remain constant.The periodic CST simulation results are used to determine the reflection-phase response for each configuration, and the frequency at which this response is zero is found. The unit cell is simulated with unit-cell boundary conditions and a Floquet port at normal incidence ($\theta = \varphi = 0°$), and the reflection phase is recorded from 1 to 10 GHz at 1001 points (9-MHz step) using frequency domain solver and tetrahedral mesh.

The zero-degree crossing frequencies extracted from the reflection-phase responses of the 216 geometries are plotted against A, G and S in Fig. 7. The results illustrate that the AMC resonance is affected by the change of each geometrical parameter and thus is altered to the frequency that the reflection phase crosses 0°. Below 3.5 GHz the trends agree qualitatively with the equivalent-LC interpretation of Section 3.2: f_0 decreases with A (up to A = 16 mm), increases with G and decreases slightly with S.



(a) (b) (c)

Fig. 7. Zero-degree crossing frequency f_0 of the 216 AMC geometries versus (a) variation of patch width A; (b) variation of inter-slot gap G; (c) variation of slot width S.

4. Machine-Learning-Assisted Inverse-Design Methodology

4-1- Overall Machine-Learning-Assisted Design Framework

The traditional electromagnetic design problem is to define a given geometry and simulate the electromagnetic response throughout it. The proposed approach includes firstly obtaining the relationship between the main geometric parameters and the electromagnetic responses from CST-based simulation. Supervised machine-learning models are then trained to approximate these relationships, and used for fast predictions during the inverse-design search.

The input for the antenna design are dimensions of the meander are a and b, and the outputs are its resonant frequency f_r and the minimum reflection coefficient S_{11},min; $S_{11}(f)$ response is also predicted. The forward relationship of the AMC is a mapping from (A, S, G) to the zero-degree reflection-phase crossing frequency f_0; the inverse of this relationship is not unique, since there are many different combinations of A, S and G that give the same f_0 (Section 3.3). The two are initially designed for $f_r \sim f_0$. Since the

electromagnetic coupling between the radiator and the finite AMC array may alter the antenna response, the final antenna–AMC design is validated with full-wave CST simulation.

The entire procedure of antenna design is as follows: (1) electromagnetic data generated by CST; (2) extraction of the desired antenna and AMC response parameters; (3) preprocessing and partitioning of the datasets; (4) training and evaluation of the following supervised-learning models; (5) surrogate-assisted inverse search or AMC geometry initialization; and (6) full-wave CST verification of the selected antenna–AMC configuration.

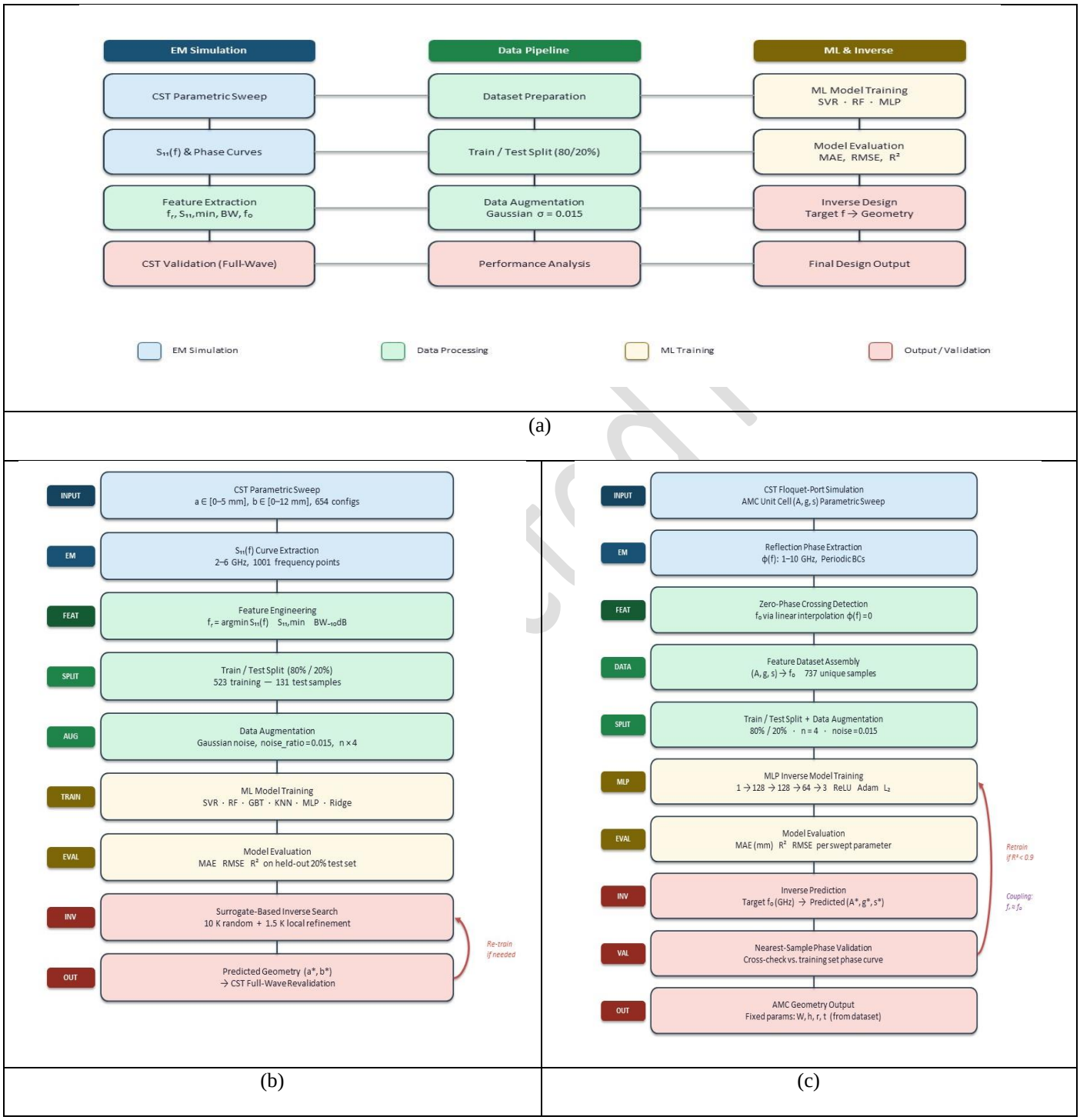


Fig. 8. Proposed inverse-design framework: (a) full data and validation; (b) antenna surrogate-model pipeline; (c) AMC inverse-model pipeline.

4-2- CST Data Generation and Feature Extraction

To create the antenna dataset, the structured CST parametric sweep described in Section 2 is used. The two main geometrical variables (a and b) are changed in the following ranges: 0–5 mm and 0–12 mm, respectively, while all the other geometrical and material variables are fixed (except s_γ in three runs; Section 2.4). After removing duplicates, the sweep results in 654 different antenna designs.

The AMC data is derived from an independent periodic CST configuration (as specified in Section 3). The three principal variables of the AMC are A, S and G while the periodicity of the unit-cell, the thickness of the substrate and others are the fixed parameters. The reflection-phase response of the simulated AMC geometry is analyzed for every geometry and zero crossing frequency f_0 is found.

Table 3. Dataset Statistics for Antenna and AMC Parametric Sweeps.

Property	Antenna Dataset	AMC Dataset
Swept parameters	a (0–5 mm), b (0–12 mm); w = 4 mm and gndy = 5 mm fixed	A (10–17 mm), G and S (0.5–3.0 mm); WS = 22 mm, h = 1.6 mm and t = 0.035 mm fixed
Total samples	654 unique geometries	216 unique AMC samples
Frequency range	2.0–6.0 GHz	1.0–10.0 GHz (f_0 searched in 2.0–6.0 GHz)
Target features	f_r, S_{11},min, BW, $S_{11}(f)$	f_0 (zero-phase crossing)
Train/Test split	80% / 20% (523/131)	80% / 20% (172/44)
Augmentation	None	Gaussian, noise_ratio=0.015

4-2-1- Antenna response extraction

For each antenna geometry, the frequency of the minimum of the simulated $S_{11}(f)$ response is the resonance frequency (f_r), the value of the minimum (S_{11},min) and the −10-dB impedance bandwidth, BW = f_high − f_low, of the $S_{11}(f)$ response where $S_{11} \leq -10$ dB, are reported and the entire $S_{11}(f)$ response is also saved for full-spectrum surrogate modeling.

4-2-2- AMC reflection-phase extraction

The zero degree reflection phase crossing is calculated from two adjacent frequency samples for each of the AMC geometries. Suppose the two frequency samples are f_1 and f_2, the phase of reflection of each of them is φ_1 and φ_2 respectively. If the phase of φ_1 and φ_2 are on opposite sides of the zero-phase crossing, then the frequency of the zero-phase crossing is estimated by using linear interpolation as follows:

$$f_0 = f_1 + \frac{0-\varphi_1}{\varphi_2-\varphi_1}\left(f_2 - f_1\right) \quad (4)$$

This interpolation enables a scalar representation of the AMC reflection-phase response, which can be used for subsequent ML analysis. The simulated reflection phase is from 1 to 10 GHz and the crossings are searched between 2 and 6 GHz. In this window the detector detects 1-5 signs changes per geometry (mean = 3.4, total = 737), but 219 of these are "±180° phase wraps" rather than 0° crossings because it is assumed that every sign change of φ is a 0° crossing (according to Eq. (4)). Only the lowest frequency that occurs in the window is selected and applied to all samples in the same manner, yielding 216 (f_0, A, S, G) tuples, one for every geometry. This rule provides one label per geometry, this is what is needed in the inverse model, as the 737 events would offer up to 5 different f_0s for the same geometry, the lowest crossing is the first AMC resonance, aligned to the antenna band. For three geometries (A = 16 mm, G = 0.5 mm), the lowest event is a ±180° wrap near 2.03 GHz. The impact of the use of all 737 events is quantified in Section 6.5 (Table 8).

4-3- Data Preprocessing, Partitioning, and Augmentation

The antenna dataset is split up into an 80:20 train-test split, with 523 train samples and 131 held-out test samples (random split, scikit-learn random_state = 42; the AMC dataset is split in the same way into 172 and 44 samples). The test data set will not be used for model construction, hyperparameter selection, or augmenting the data set. The hyperparameters of all models are pre-determined (Table 4), the surrogate is chosen by five-fold cross validation of the training set (Section 4.4) and the test set is not used until the end to report the final accuracy. To test whether there is generalization beyond a single random split, the models are also tested over

Uncorrected Proof

20 repeated random 80:20 splits, and with a geometry-blocked cross-validation, where the (a, b) plane is split into 5 × 5 blocks of 1 mm × 2.5 mm and whole blocks are withheld (Section 6.1).

The input features are scaled using only the statistics computed from the training set for a machine-learning model that is sensitive to the scale of its input variables. The input to be standardized is

$$x_{\text{scaled}} = \frac{x - \mu_{\text{train}}}{\sigma_{\text{train}}} \tag{5}$$

where μ_train and σ_train are the mean and standard deviation of the feature from the training subset respectively.

This transformation is then applied to the test data and new geometries can be given as inputs for inferences. Since decision rules of trees do not require conventional feature standardization, original feature scale will be used for tree-based models. Data augmentation is used only for the AMC models with data augmentation applied to only the training split of the data. Four copies of each AMC training sample are generated, with Gaussian noise with zero mean and standard deviation σ = 0.015 × (range of all the inputs in the training split) added to the inputs of each copy (NumPy random generator, seed 42) and no noise added to the outputs. This can be seen to result in an estimated value of σ of approximately 48 MHz on f_0 in the inverse MLP and σ of 0.105 mm in the forward multilayer preceprtron (MLP) and σ of 0.105 mm for A and 0.0375 mm for G and S). Physically consistent in that the geometric perturbations are about one tenth of the sweep steps (1 mm for A and 0.5 mm for G and S) and with the sensitivities of Section 6.2, shift f_0 by only about 1-14 MHz, which is of the order of the 9-MHz frequency step of the phase data; the f_0 perturbation (approx. 48 MHz) is smaller than the median f_0 change between neighbouring grid geometries in A (approx. 78 MHz) and G (approx. 142 MHz). The impact of it is measured in Section 6.5 (Table 8).

4-4- Machine-Learning Model Development and Evaluation

A total of eight supervised-learning algorithms are tested: Linear Regression, Ridge Regression, Support Vector Regression (SVR), k-Nearest Neighbors (KNN), Multilayer Perceptron (MLP), Decision Tree, Random Forest and Gradient Boosting. Their settings are listed in Table 4.

Table 4. Settings of the machine-learning models and inverse searches.

Model	**Inputs**	**Settings**
Linear regression	a, b (standardized)	Ordinary least squares
Ridge regression	a, b (standardized)	α = 1.0
SVR	a, b (standardized)	RBF kernel, C = 100, γ = 'scale', ε = 0.01
KNN	a, b (standardized)	k = 5, uniform weights, Euclidean distance
Decision tree	a, b (raw)	Fully grown (no depth limit), random_state = 42
Random forest	a, b (raw)	250 trees, bootstrap sampling, random_state = 42
Gradient boosting	a, b (raw)	100 trees, learning rate 0.1, maximum depth 3, squared-error loss, random_state = 42
MLP (antenna)	a, b (standardized)	Hidden layers 128–64–32, ReLU, Adam (learning rate 0.001, mini-batch 200), L_2 penalty $\alpha = 10^{-4}$, early stopping on 15% of the training data (patience 80 epochs, at most 3000 epochs), random_state = 42
$S_{11}(f)$ curve model	a, b (raw)	Multi-output random forest: one 120-tree forest per frequency point (1001 outputs), random_state = 42
AMC inverse MLP	f_0 (standardized)	Hidden layers 128–128–64, ReLU, Adam (learning rate 0.001, mini-batch 200), $\alpha = 5 \times 10^{-4}$, early stopping on 15% (patience 60 epochs, at most 5000 epochs), random_state = 42; outputs A, G, S in mm
AMC forward MLP	A, G, S (standardized)	As the AMC inverse MLP; output f_0 in GHz
Antenna inverse search	SVR (f_r, S_{11},min)	15 000 uniform + 3000 local Gaussian candidates (σ = 5% of range); feasible if $\lvert f_r - f_t \rvert \le 0.03$ GHz and $S_{11,\min} \le S_{11,t}$; λ = 0.05
AMC inverse search	Forward MLP	10 000 uniform candidates (including the inverse-MLP seed) + 4 × 1500 local candidates (initial radius 15% of range, shrink factor 0.35)

Unconnected Proof

The tree based models are trained with the original feature scale while standardised input variables are used in Linear Regression, Ridge Regression, SVR, KNN and MLP. The most important scalar predictions are the antenna resonant frequency f_r, and the minimum value of the reflection coefficient S11,min. The whole $S_{11}(f)$ response is judged independently, based on the chosen full-spectrum surrogate model.The mean absolute error, MAE = $(1/N)\ \Sigma|y_i - \hat{y}_i|$, the root mean square error, RMSE = $\sqrt{[(1/N)\ \Sigma(y_i - \hat{y}_i)^2]}$, and the coefficient of determination, $R^2 = 1 - \Sigma(y_i - \hat{y}_i)^2/\Sigma(y_i - \bar{y})^2$, where y_i is the CST value of the i-th of the N test samples, $\hat{y}_i$ its ML prediction and $\bar{y}$ the mean of the y_i are the three metrics used to measure the predictive performance of the ML models.

Model selection is done based on the mean MAE of each prediction target in five-fold cross-validation on the training set; the held-out test set is not used for this choice. The best performing model in terms of prediction is then selected as the surrogate for the inverse-design task. The numerical comparison and choice of the best performing model is not reported in methodology, but instead in Section 6.

5. Machine-Learning-Assisted Inverse Design and GUI

5-1- Antenna Inverse Design by Surrogate-Based Search

The trained forward surrogate is employed to solve the inverse antenna-design problem without computing all the candidate geometries with the full-wave solver. The goal is to find the values of the antenna size parameters, a and b, which yield a resonant frequency near the desired value, and meet the desired matching criterion for the antenna impedance.

Geometries are generated in the range of the CST parametric sweep. Those candidates that fail to meet the prescribed S_{11} criteria are disqualified. The other candidates are ranked by the resonance error and a compactness term.

$$J(a,\ b) = \left| f_r(a,\ b) - f_t \right| + \max\left[0,\ S_{11,\min}(a,\ b) - S_{11,t}\right] + \lambda \frac{a+b}{(a+b)_{\max}} \qquad (6)$$

where $f_r(a,b)$ is the surrogate-predicted resonant frequency, f_t is the target resonant frequency, and λ is a weighting coefficient that dictates how close to the compact geometries or not. If f_r is measured in GHz and a and b in millimetres then λ will have the units needed to ensure consistency of dimensionality. The second term is meant to punish candidates who fail to meet the impedance-matching requirement, and the compactness term (a+b) is rescaled by its maximum value across the candidate pool so that candidates can be compared against each other. The S_{11} spectrum of the selected candidate is then predicted with the multi-output random-forest model (Section 6.3), and the candidate is sent to CST for the final electromagnetic verification.

5-2- AMC Inverse Geometry-Initialization Model

The AMC inverse-design stage is used to find a unit-cell geometry that results in a zero-degree reflection-phase crossing frequency for a specified value. From the forward relationship defined in Section 3, the AMC response could be modeled as a nonlinear function of A, S and G to the extracted zero phase frequency f_0. For inverse design, the target frequency is supplied to an MLP that predicts the three geometric variables.

The implemented MLP uses the architecture $1 \rightarrow 128 \rightarrow 128 \rightarrow 64 \rightarrow 3$. ReLU activation functions are used in the hidden layers. The model is trained with the standard input processing, Adam optimisation, L_2 regularisation ($\alpha = 5 \times 10^{-4}$) and early stopping (15% validation split, 60-epoch patience) on the augmented AMC training set. The variables predicted are limited to the geometry range included in the training data. Each parameter is limited separately, so combinations outside the simulated region (for example a large S at a small A) are possible. In the GUI, the MLP output also seeds a random search (10 000 global and 4 × 1500 local candidates) that uses a second, forward MLP (A, S, G → f_0) to select the geometry whose predicted f_0 is closest to the target.

The MLP output is hence not generally a unique inverse solution, but rather an initial candidate geometry. Thus the geometry predicted for the AMC needs to be subjected to CST reflected phase verification.

5-3- Initial Antenna–AMC Separation and Coupled Optimization

The phase condition for constructive interference between the radiation directly from the antenna and the field reflected from the AMC surface is used to estimate the initial separation between the antenna and AMC. The following phase condition was employed in the design procedure:

Uncorrected Proof

$$2kd - \varphi_{\Gamma}(f) = 2m\pi \tag{7}$$

In which f is the operating frequency, k is the free space wavenumber, d is the distance between the antenna and the AMC, φ_Γ(f) is the AMC reflection phase at the operating frequency and m is an integer indicating the selected phase branch. The initial separation for a chosen branch is given by

$$d = \frac{\varphi_{\Gamma}(f) + 2m\pi}{2k} \tag{8}$$

The separation value calculated is only an initial value. The optimum spacing is obtained from a limited number of full wave CST simulations, since the analytical phase relation is not a complete solution of the problems due to the finite AMC size, antenna interaction, antenna and AMC substrate interaction, and the complete three dimensional electromagnetic environment. The right integer m is picked to ensure that the separation is within the physically realizable range of separations that are currently modeled in the CST model.

For example, at f = 2.4 GHz (k = 50.3 rad/m) the reflection phase of the final unit cell in Fig. 6 is about +140° (2.44 rad) and the CST simulation data gives approx. +157.9°, which gives d ≈ 2.44/(2 × 50.3) ≈ 24 mm for m = 0. This estimate was only made as a starting point, since the phase changes rapidly around 2.4 GHz, and K = 10 mm was derived from CST simulations.

The optimized sequence is thus (i) prescribe target frequency and matching constraint, (ii) get antenna candidate, (iii) get AMC candidate, (iv) estimate spacing between the antenna and AMC, (v) build the full antenna–AMC, (vi) optimization in CST, and (vii) choose the configuration that meets the specified electromagnetic constraints.

5-4- Automated Implementation Using the GUIs

All the workflow is done through a GUI implemented in Python. The GUI acts as an automation layer between the data processing of CST, Model Training, Inverse Prediction, and response visualization. It is not an independent electromagnetic solver.

The interface automatically handles the parameter data for the CST, determines swept and fixed variables, processes the data through the desired data-processing routines, trains the desired machine-learning models, provides model-performance results, takes in the target design requirements, and delivers candidate geometries and predicted responses.

The GUI can load a CST dataset, identify the parameters, perform preprocessing on the CST dataset, train a model from the CST dataset, set the target-frequency and perform a surrogate-based inverse search for it, and visualize the response for the target-frequency. It can be used for loading of the dataset, identification of A, S and G, training MLP, setting the desired f_0, predicting a candidate geometry and generating a visualization of the reflection-phase.

6. Results and Discussion

6-1- Forward Surrogate-Model Performance

The eight supervised-learning models are tested on an independent test set of 131 antennas. The models give the values f_r and S_{11},min where a and b are the two geometric variables. Table 5 includes the whole numerical comparison including the value of MAE, RMSE and R^2.

Table 5. Performance of the machine-learning models on the held-out antenna test set (131 samples).

Model	**f_r MAE (GHz)**	**f_r RMSE (GHz)**	**f_r R^2**	**S_{11},min MAE (dB)**	**S_{11},min R^2**
SVR	0.00519	0.00620	0.99980	0.248	0.9441
MLP	0.01177	0.01631	0.99860	0.293	0.9435

Uncorrected Proof

Random Forest	0.01382	0.01896	0.99811	0.325	0.9393
Gradient Boosting	0.01596	0.02084	0.99771	0.380	0.9395
KNN	0.01662	0.02427	0.99690	0.407	0.9391
Decision Tree	0.03618	0.04297	0.99029	0.558	0.9340
Ridge	0.05872	0.08294	0.96381	1.104	0.8917
Linear Regression	0.05877	0.08281	0.96392	1.107	0.8917

As can be seen from the numerical results seen in Table 5, the SVR model has obtained the smallest error in the calculation of the resonant frequency from the 8 models, namely the error MAE = 0.00519 GHz (5.2 MHz), the error RMSE = 0.00620 GHz, and R^2 = 0.99980. The next two models for the resonant frequency, namely MLP and Random Forest, have higher errors. The same trend is seen with S_{11},min, where SVR has the lowest MAE of 0.248 dB, and the highest R^2 of 0.9441. Therefore, a statistical comparison shows that SVR is the best scalar surrogate of the two antenna outputs.

The linear models have significantly higher errors, suggesting that a linear geometry-to-resonance relationship will not suffice for this meander-line structure. For S_{11},min, the differences between the nonlinear models are less pronounced than those of resonance frequency, but the error of SVR is still the lowest.

For the resonant frequency model, the SVR R^2 value is almost 1 (0.99980), which indicates that almost all the variance in the held out CST resonant frequency values is explained by the model. For S_{11},min, the maximum R^2 is lower at 0.9441. This means that there is a physical difference between the resonance frequency and the depth of the minimum of the reflection coefficient: The resonance frequency is more a function of the effective electrical length, while the depth of the minimum of the reflection coefficient is more a function of the impedance matching and the coupling. Thus, it may be inferred that the models can predict the resonance more consistently than exactly the depth of the minimum of S_{11}.

Table 5 reveals that the value of MAE for SVR is the lowest and that of R^2 is the highest for both the outputs and the value of RMSE is the lowest for f_r; hence, it is chosen as a scalar forward surrogate for the antenna inverse design.

A random split was used to obtain these values. Five-fold cross validation is done on the training set alone and the model choice is confirmed, while also demonstrating its robustness to the split, as seen in Table 6 for 20 repeated random splits, and for the geometry-blocked cross validation. In all of these 20 random splits, the lowest MAE is for SVR (5.5 ± 0.5 MHz for f_r, consistent with the value in Table 5, which has a 95% bootstrap interval of 4.6–5.8 MHz, and close to the 4-MHz frequency step of the simulation), and in the blocked test, in which every geometry predicted is a region not used for training (11.7 ± 1.8 MHz against 72 MHz for Random Forest). The S_{11},min MAE of 0.248 dB is dominated by one test geometry simulated with s_γ = 32 mm (Section 2.4); without it, the MAE is 0.128 dB and R^2 = 0.9986. The SVR achieves a mean R^2 of 0.9938 and a range of 0.9812-0.9991, and an f_r MAE of 18.3 MHz, with just 10% of the training data (52 samples, 20 random subsets) compared with 5.2 MHz with the full training set. All samples are from a single simulation grid and no independent data exists, so these results are only applicable in the swept (a, b) domain.

Table 6. Robustness of the eight antenna models: mean ± standard deviation of the test MAE and R^2 over 20 repeated random 80:20 splits, and of the out-of-fold MAE in geometry-blocked five-fold cross-validation (ten repetitions).

Model	**f_r MAE (MHz) random splits**	**f_r R^2 random splits**	**f_r MAE (MHz) blocked CV**	**S_{11},min MAE (dB) random splits**	**S_{11},min R^2 random splits**	**S_{11},min MAE (dB) blocked CV**
SVR	5.5 ± 0.5	0.9997 ± 0.0001	11.7 ± 1.8	0.16 ± 0.05	0.986 ± 0.024	0.20 ± 0.01
MLP	11.7 ± 1.2	0.9984 ± 0.0004	24.2 ± 3.2	0.27 ± 0.06	0.984 ± 0.024	0.46 ± 0.06
Random Forest	12.6 ± 1.3	0.9977 ± 0.0005	71.8 ± 12.3	0.22 ± 0.05	0.986 ± 0.023	0.92 ± 0.15

Unedited Proof

Model	f_r MAE (MHz) random splits	f_r R^2 random splits	f_r MAE (MHz) blocked CV	S_{11},min MAE (dB) random splits	S_{11},min R^2 random splits	S_{11},min MAE (dB) blocked CV
Gradient Boosting	11.8 ± 1.8	0.9984 ± 0.0005	58.7 ± 7.3	0.27 ± 0.05	0.985 ± 0.023	0.81 ± 0.12
KNN	14.3 ± 1.5	0.9971 ± 0.0008	60.6 ± 5.6	0.32 ± 0.05	0.980 ± 0.023	0.92 ± 0.11
Decision Tree	33.2 ± 1.9	0.9908 ± 0.0010	82.7 ± 8.4	0.45 ± 0.05	0.981 ± 0.023	1.12 ± 0.14
Ridge	54.6 ± 3.7	0.9664 ± 0.0052	63.3 ± 2.1	1.14 ± 0.08	0.918 ± 0.026	1.30 ± 0.12
Linear Regression	54.7 ± 3.7	0.9663 ± 0.0052	63.4 ± 2.2	1.14 ± 0.08	0.918 ± 0.026	1.30 ± 0.12

6-2- Parametric Sensitivity Analysis

The results of the model-comparison provide a measure of predictive accuracy, but do not on their own explain how the physical parameters influence resonance. It is therefore proposed to use the CST sweep to estimate the local sensitivity of f_r to the two antenna variables at the chosen reference geometry.

$$\frac{\partial f_r}{\partial a} \approx -0.07 \text{ GHz/mm}, \quad \frac{\partial f_r}{\partial b} \approx -0.06 \text{ GHz/mm} \tag{9}$$

Based on the illustrations in Fig. 9 both sensitivities are negative which means that increasing either of the geometric parameters will result in a decrease of the local resonant frequency. The magnitude of $\partial f_r/\partial a$ is about 1.2 times that of $\partial f_r/\partial b$, so near the reference geometry a gives a slightly larger frequency change per millimetre than b. Over the whole grid the sensitivities are larger (medians of −0.13 and −0.084 GHz/mm) and grow towards small a and b. This is local, and must not be interpreted as being the case for a constant derivative throughout the parameter domain.

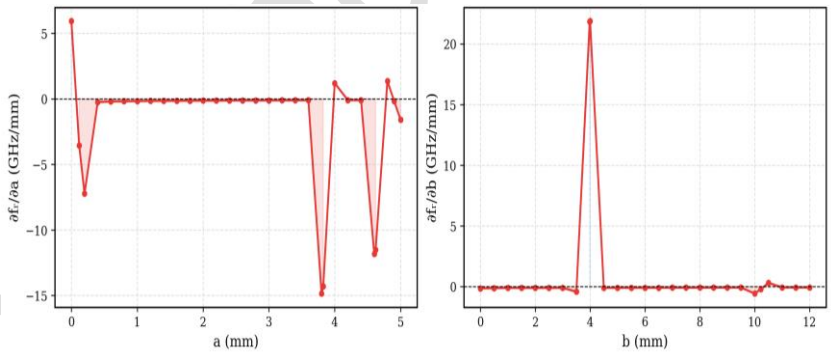


Fig. 9. Local antenna-parametric sensitivities $\partial f_r/\partial a$ and $\partial f_r/\partial b$ computed from the CST sweep at the selected reference geometry.

In a similar way, a sensitivity analysis is performed for the AMC parameters A, G and S at a zero degree reflection-phase crossing frequency f_0 . The influence of the three parameters is different with respect to the slope, the mean f_0 increases steadily with G, while the influence of A and S is non-monotonic; for S = 3 mm the dependence is monotonic. As predicted in Section 3.2, f_0 decreases with increasing A (2.80 to 2.26 GHz for A = 10-16 mm), increases with increasing G (2.17 to 3.07 GHz) and decreases slightly with increasing S (approx. −0.03 GHz/mm for fixed A and G), all of which are confined to the crossings below 3.5 GHz. The AMC response is thus not governed by any one of the parameters. This is helpful for the use of a multivariable surrogate/inverse model for AMC geometry generation.

6-3- Full-Spectrum S_{11} Prediction

The forecasting of just f_r and S_{11},min does not result in the full impedance response. The sampled S_{11} spectrum is then predicted over 2–6 GHz using a multi-output Random Forest model of a and b.

Uncorrected Proof

$$\mathbf{Y} = \left[S_{11}(f_1),\ S_{11}(f_2),\ \ldots,\ S_{11}(f_N) \right] \tag{10}$$

A representative set of test samples were compared with the predicted spectra in Fig. 10 showing the corresponding CST curves. The predicted curves are able to reproduce the principal resonance, the approximate minimum value, and the overall shape of the spectrum. Over the 131 test samples the curve-level MAE is 0.25 dB (95% bootstrap interval 0.23–0.28 dB) and the RMSE 0.65 dB (0.60–0.69 dB). This result is significant for inverse design since the candidate geometry needs to be tested based on its spectral behavior and not just one resonance frequency.

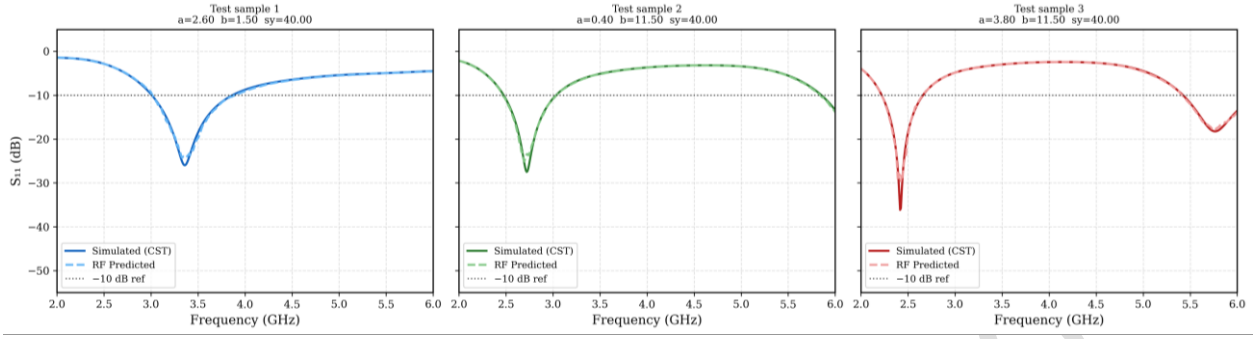


Fig. 10. Multi-output S_{11}-curve prediction for three representative test samples: comparison of CST-generated and random-forest-predicted responses.

6-4- Antenna Inverse-Design Result

Then the trained SVR is used for surrogate-assisted inverse search. The values of a and b are created in the CST training domain and verified against the desired resonance and impedance matching. This candidate is then taken to CST for full verification (or full check against full wave).

For the quantitative validation, the search was performed for five frequencies (2.40 – 4.00 GHz) and the search was also performed for stricter matching requirement and the feasible candidates were re-simulated in CST (Table 7). All the frequency targets provide feasible candidates and due to the most compact feasible candidate being selected the predicted f_r is towards the top of the range within the ±30 MHz tolerance. CST data is also shown which shows almost in agreement with the predicted data.

Table 7. Antenna inverse design for several targets.

f_t (GHz)	S_{11},t (dB)	a (mm)	b (mm)	SVR f_r (GHz)	SVR S_{11},min (dB)	CST f_r (GHz)	CST S_{11},min (dB)	CST S_{11},f_t (dB)	$\lvert f_r$,CST − $f_t \rvert$ (MHz)
2.40	−10	4.780	10.065	2.430	−38.8	2.44	-50	-22	40
2.70	−10	4.662	5.675	2.730	−37.2	2.74	-46.2	-26	40
3.00	−10	5.000	1.518	3.030	−30.8	3.024	-35.4	-30	24
3.50	−10	2.434	0.000	3.530	−23.8	3.54	-24.8	-23.8	40
4.00	−10	0.432	0.000	4.030	−19.4	4.036	-20	-19.9	36

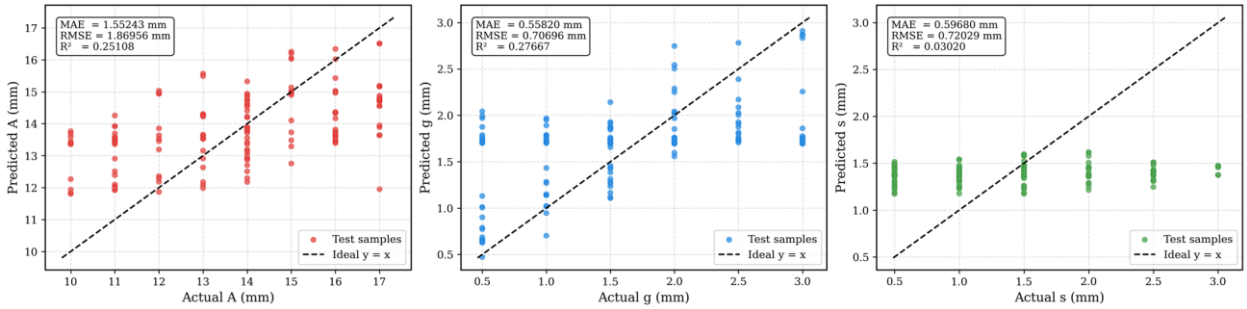
6-5- AMC Inverse-Design Performance

The target zero-degree reflection-phase frequency f_0,t is given to the AMC inverse MLP for prediction of A, S, and G. Since the inverse problem is not unique, the predictions are not unique solutions to the problem, but rather are starting guesses for the geometry.

The predicted and actual values of the three AMC geometric parameters were compared as shown in Fig. 11. The spread of the data points from the ideal y=x line reflects the degree of accuracy by which the data point is predicted for each parameter. It also shows the different predictability of A, S and G, and matches the parameter-wise MAE and R^2 results that are described later.

Uncorrected Pro

10.22060/EEJ.2026.26568.6160



(a) (b) (c)

Fig. 11. AMC inverse-MLP results: predicted versus actual values for (a) patch width A, (b) inter-slot gap G, and (c) slot width S.

The training process is carried out for 429 epochs, where a low plateau in the validation score (R^2 on 15% early stopping split) is reached and the weights of the best validation epoch are used; the small value of the validation score (≈0.41) is due to the non-uniqueness of the inverse mapping.

The inverse MLP, with one crossing per geometry (216 samples, 172 for training and 44 for testing), produces test MAEs of 1.54 mm, 0.44 mm and 0.58 mm, and test R^2 of 0.28, 0.53 and 0.04 for the A, G and S, respectively (Fig. 11). For comparison, the same network trained on all 737 in-band sign changes gives MAEs of 1.55, 0.56 and 0.60 mm and R^2 values of 0.25, 0.28 and 0.03. Over 20 random splits (Table 8), the MAEs are 1.32, 0.42 and 0.62 mm with the 216 labels and 1.53, 0.58 and 0.61 mm with the 737 labels; when both models are tested on the lowest crossing of the same unseen geometries, the difference is smaller (1.34, 0.43 and 0.60 mm against 1.39, 0.44 and 0.59 mm). So the removal of the crossing-multiplicity ambiguity results in a better prediction of A and G and S is essentially not determined by f_0 alone ($R^2 \approx 0$). This is mostly due to the fact that the three parameters of the geometry are given by a single scalar, f_0, and the mixed labelling of Section 4.2.2 makes for some scatter. However, the forward MLP used by the GUI for screening candidates (A, S, G → f_0) only has a test R^2 of 0.11 (MAE 0.64 GHz) on the same split (0.31 ± 0.18 over 20 random splits) and it is therefore a rough consistency check only: for a target of 2.40 GHz, ten random seeds of the search give A = 10.0–14.8 mm, G = 0.8–2.2 mm and S = 0.8–2.9 mm, each with a forward-predicted f_0 of 2.400 GHz. The inverse-MLP MAEs without the augmentation of Section 4.3 are 1.34, 0.43 and 0.63 mm (Table 8), (i.e. the augmentation acts only as a mild regularizer).

Table 8. AMC inverse-MLP test accuracy for the two label definitions and for the augmentation ablation.

Labels and augmentation	**Samples**	**MAE A**	**MAE G**	**MAE S**	**R^2 A**	**R^2 G**	**R^2 S**	**Forward-MLP R^2**
Lowest crossing per geometry; noise 0.015 × range (used)	216	1.32 ± 0.08	0.42 ± 0.06	0.62 ± 0.05	0.44 ± 0.09	0.57 ± 0.13	0.01 ± 0.10	0.31 ± 0.18
All in-band events; noise 0.015 × range	737	1.53 ± 0.06	0.58 ± 0.03	0.61 ± 0.03	0.26 ± 0.04	0.29 ± 0.05	0.01 ± 0.03	—
Lowest crossing; no augmentation	216	1.34 ± 0.10	0.43 ± 0.06	0.63 ± 0.05	0.43 ± 0.08	0.55 ± 0.15	0.00 ± 0.08	0.25 ± 0.17
Lowest crossing; noise 0.030 × range	216	1.32 ± 0.08	0.42 ± 0.06	0.63 ± 0.05	0.44 ± 0.09	0.57 ± 0.13	0.01 ± 0.10	0.28 ± 0.18
Grouped splits: trained on lowest crossings, tested on lowest crossings of unseen geometries	216	1.34 ± 0.16	0.43 ± 0.04	0.60 ± 0.06	0.46 ± 0.09	0.56 ± 0.11	−0.06 ± 0.14	—
Grouped splits: trained on all events of the training geometries, same test labels	737	1.39 ± 0.19	0.44 ± 0.04	0.59 ± 0.06	0.42 ± 0.10	0.54 ± 0.09	−0.01 ± 0.06	—

The AMC search was conducted for seven frequencies of interest in the range 2.40 GHz to 5.40 GHz and the chosen set of unit cells were re-simulated in CST (as shown in Table 9). Predictions by the forward MLP are almost always very close to the target f_0 and do not provide an independent check of the AMC inverse design; the CST f_0 is the actual one and is in close agreement with predicted ones.

Uncorrected Proof

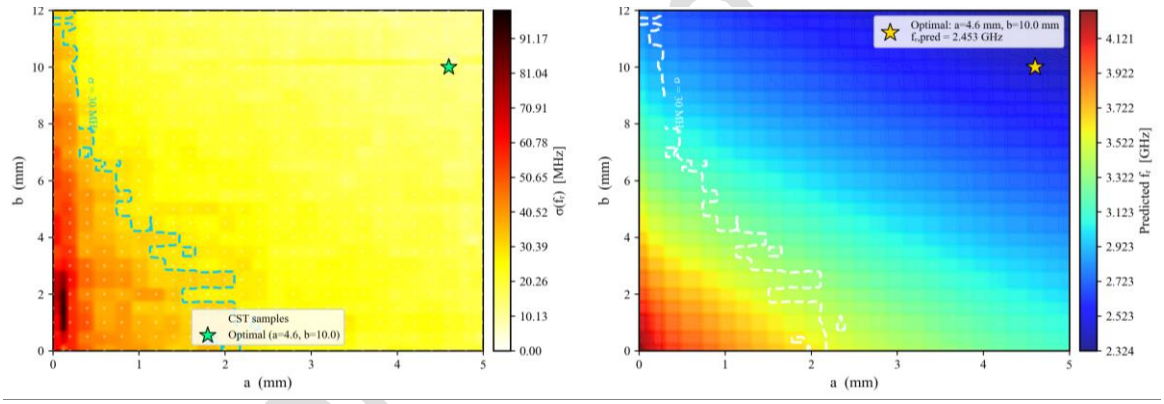
Table 9. AMC inverse design for several target frequencies.

$f_{0,t}$ (GHz)	A (mm)	G (mm)	S (mm)	Forward-MLP f_0 (GHz)	CST f_0 (GHz)	CST zero degree reflection phase at f_t (degree)	$\lvert f_{0,CST} - f_{0,t} \rvert$ (MHz)
2.40	10.13827	0.551604	1.523630	2.400	2.41	10.7	10
4.40	16	3	0.5	4.4382	4.4278	+2.29	27.8
4.60	15	2.5	2	4.6100	4.5954	-0.44	4.6
4.80	17	3	1	4.7268	4.8086	+0.45	8.6
5.00	13	3	2	5.0150	4.9964	-0.15	3.6
5.20	10	3	1.5	5.2298	5.1999	-0.00	0.1
5.40	16	1	2	5.3777	5.3988	-0.05	1.2

6-6- Prediction Uncertainty

The level of reliability is not the same in the design area for prediction accuracy. Empirical uncertainty is thus estimated as the dispersion of individual tree predictions, by using a Random Forest ensemble. The predicted value of the standard deviation $\sigma(f_r)$ is plotted in Fig. 12(a) and the resonance frequency surface is plotted in Fig. 12(b).

The predicted standard deviation ranges from 8.3 to 98.4 MHz; it stays below 30 MHz over 81.1% of the design region and is largest along the small-a boundary. The uncertainty map thus shows areas where the surrogate is well supported by the training data sets, and areas in which the CST verification effort should be given greater priority.



(a) (b)

Fig. 12. Random Forest prediction uncertainty for resonant frequency: (a) $\sigma(f_r)$ over the antenna design space; (b) predicted f_r surface with the reference geometry indicated.

6-7- Coupled Antenna–AMC Impedance Response

The last system level validation is a comparison of the standalone antenna and the AMC supported antenna. The physical topology used for the coupled CST simulation is depicted in Fig. 13, the antenna is located above the finite AMC surface with K = 10 mm. This number must match exactly the geometry which is used to produce the next electromagnetic results. The coupled model is simulated with a time domain solver,Hexadral FIT mesh , open boundary conditions and waveguide port.

Uncorrected Proof

10.22060/EEJ.2026.26568.6160



(a) (b)

Fig. 13. AMC-backed antenna topology in free space; (a) top View, (b)side view.

A comparison of the simulated S_{11} of the two configurations is shown in Fig. 14. The standalone antenna has a resonance around 2.41 GHz and a deep minimum (approx. −60 dB) and a −10 dB bandwidth of about 430 MHz (approx. 2.22–2.64 GHz). With the AMC, S_{11} at 2.4 GHz is −13.1 dB (−34.3 dB without the AMC), the minimum in the 2.4 GHz band moves to about 2.50 GHz (about −15 dB; the deepest minimum of this curve, about −26 dB, is near 5.7 GHz) and the −10 dB bandwidth narrows to about 260 MHz (approx. 2.32–2.58 GHz). As a result, the AMC can move the resonance up some 90 MHz and narrow the bandwidth by some 40%, without losing the match in the 2.4 GHz band below −10 dB.

The change in resonance is expected because the system (AMC-backed) is a coupled electromagnetic system. Therefore, starting point for design is the isolated antenna resonance and also the isolated AMC phase crossing, and the final integrated S_{11} response in Fig. 14 is the desired resonating behavior.

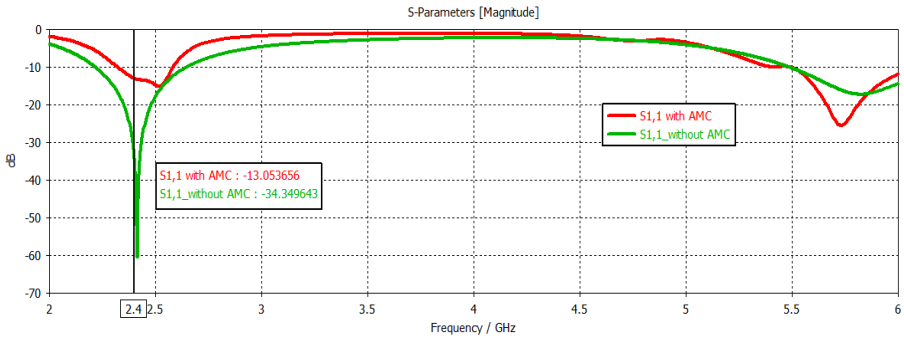


Fig. 14. Simulated S_{11} comparison between the standalone antenna and the AMC-backed antenna, showing the resonance location and −10-dB impedance bandwidth.

6-8- Gain, Directivity, and Radiation Efficiency

The realized gain of the standalone and AMC backed configurations are compared in Fig. 15. The gain of the standalone antenna is 1.16 dBi at 2.4 GHz, while the AMC's gain is 4.46 dBi, an improvement of 3.30 dB.

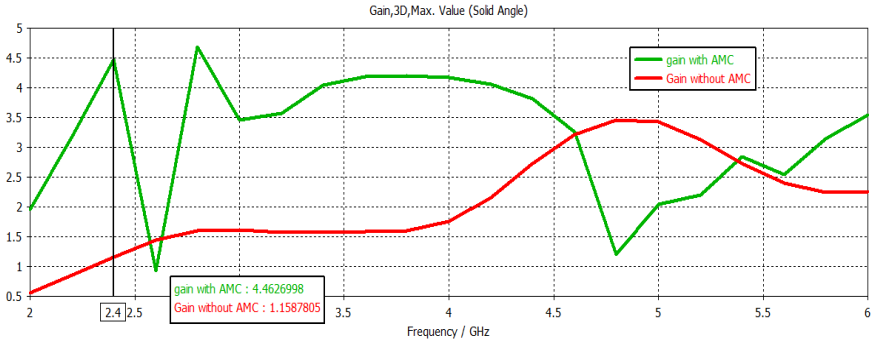


Fig. 15. Simulated realized gain of the standalone and AMC-backed antennas over frequency.

Uncorrected Proof

The gain improvement should be looked at in conjunction with directivity and radiation efficiency. The directivity is boosted from 2.23 to 6.65 dBi and the efficiency is reduced from 76.9% to 60.4% respectively. Thus, it is a gain enhancement that is mostly linked with the redistribution of the radiated field and/or increase in directivity instead of increase in radiation efficiency. This is important since a higher gain does not necessarily mean lower conductor/dielectric loss.

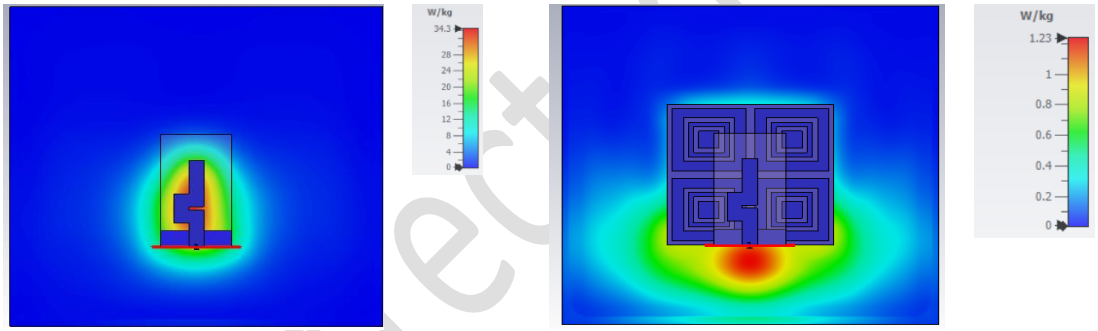
6-9- SAR Performance

The SAR is calculated at 2.4 GHz for the dielectric properties of human tissue layers as shown in Table 10. The spatial distribution of SAR is compared for the standalone and AMC supported configurations in Fig. 16.

Table 10 : Dielectric properties of human tissue layers in the 2–6 GHz frequency range used for SAR analysis.[30]

Layer	Permittivity (ε_r)	Conductivity (S/m)	Density (kg/m³)
Denim	1.781	0.083	751
Skin	41.42	0.89	1121
Fat	5.45	0.049	780
Muscle	54.88	0.959	1121

Reported maximum local 1-g SAR is 34.3 W/kg (standalone antenna) and 1.23 W/kg (AMC-backed antenna) with an input power of 100 mW. This is about 28 times lower. The distributions in Fig. 16 are for the near field that has been reduced and redistributed towards the tissue phantom.



(a) (b)

Fig.16. SAR distribution at 2.4 GHz for the 1-g averaged tissue-phantom model: (a) standalone antenna and (b) AMC-backed antenna.

The AMC-backed value is below the 1.6 W/kg limit that applies to 1-g averaged SAR [28]; this holds for the given definitions, frequency, input power, tissue properties and geometry.

6-10- Overall Electromagnetic Performance

Table 11. Overall simulated performance of the standalone and AMC-backed antennas.

Parameter	Standalone antenna	AMC-backed antenna
Resonant frequency (GHz)	2.41	2.50
−10-dB bandwidth (MHz)	430	260
Gain at 2.4 GHz (dBi)	1.16	4.46

Uncorrected Proof

Directivity (dBi)	2.23	6.65
Radiation efficiency (%)	76.9	60.4
Peak 1-g SAR (W/kg)	34.3	1.23

The principal results from the main electromagnetic are shown in Table 11. In conclusion, it can be concluded that the reported 1-g SAR is reduced from 34.3 W/kg to 1.23 W/kg and, at the same time, a system level benefit of the AMC for the considered antenna configuration is established and a trade-off between the directivity of the antenna and its radiation efficiency and bandwidth is demonstrated, most significantly for a wearable application considered in the present work.

Table 12 is a comparison between the proposed antenna and some representative wearable antennas that have been backed by AMC (Artificial Magnetic Conductor) and that use ML. The SAR values are presented with averaging mass and input power as these vary from study to study. The gain enhancement of the proposed antenna (3.3 dB) is within range of the previous AMC-backed designs (1.4–5.3 dB) and the SAR reduction of the proposed antenna (96%) is slightly smaller (97–99%), but unlike this work, the antennas in the latter designs were also fabricated and measured. The fundamental distinction is between the two manners of design, as indicated in Section 1.

Table 12. Comparison with previous wearable antennas.

Ref.	**Band (GHz)**	**Substrate**	**AMC (array, size)**	**Gain with AMC (dBi)**	**Peak SAR with AMC (W/kg)**	**Body model**
[1]	2.4	Jeans, ε_r 1.9, 0.7 mm	2 × 2, 43 × 43 mm	7.81	0.070	Four-layer chest block and arm cylinder
[2]	2.45	Felt, ε_r 1.3, 2 mm	2 × 2, 34-mm cells	5.19	0.381	One-, three- and four-layer flat; arm
[3]	2.45 / 5.8	Felt, ε_r 1.3, 2 mm	3 × 3, 102 × 102 mm	7.02	0.138	Three-layer flat chest
[4]	2.45	Cotton, ε_r 1.6, 0.8 mm (antenna)	Circular patches, 4 × 6	7.09	0.672	Three-layer flat; spine, forelimb
[8]	2.45 / 5.8	FR-4, 0.8 mm (antenna), 1.6 mm (AMC)	3 × 3, 76.5 × 76.5 mm	3.34 / 7.48	0.118	Three-layer
[14]	2.4 / 5.8	Rogers, ε_r 3, 0.5 mm	No AMC	3.8 / 6.0	0.533	Four-layer
[16]	2.4 / 5.8	RO3003, ε_r 3, 0.5 mm	No AMC	4.0 / 6.2	1.17	Four-layer
This work	2.4	FR-4, ε_r 4.3, 1.6 mm	2 × 2, 22-mm cells	4.46	1.23	Four-layer

Uncorrected Proof

7. Conclusion

This work gave a machine learning-aided design methodology for an AMC supported wearable antenna working at the vicinity of 2.4 GHz ISM band. The 654 CST-generated samples were used to train the SVR model for the resonant-frequency prediction, and the proposed inverse-design framework helped to rapidly select the antenna and AMC geometry and then verified the electromagnetic properties of the selected geometry using CST. The AMC-driven antenna has moved the resonance from 2.41 to

2.50 GHz. The realized gain was increased from 1.16 dBi to 4.46 dBi (a 3.3 dB gain) and the reported peak 1-g SAR reduced from 34.3 to 1.23 W/kg. The results show that the AMC could simultaneously achieve improvements in the radiation performance and in the level of electromagnetic exposure for the configuration analyzed as a wearable antenna. The present results are based on simulations within the swept parameter ranges of a single dataset; fabrication, on-body measurements and an independent validation dataset are left for future work.

Authors credit

Nishant Kumar: Methodology, Software, Investigation, Writing - Original Draft, Visualization

Rashmi Sinha: Conceptualization, Resources, Validation, Supervision, Writing - Review & Editing

Declaration of competing interest

The authors declare that they have no known competing financial interests or personal relationships that could have appeared to influence the work reported in this paper.

Data Availability

The datasets used and/or analysed during the current study are available from the corresponding author on reasonable request.

REFERENCES

[1] A. Ashyap, R. Raad, F. Tubbal, W. Ali Khan, and S. Abulgasem, "A compact AMC-backed meander line antenna with low SAR and high gain for wearable ISM band applications," IEEE Access, vol. 13, pp. 151624–151640, 2025, doi: 10.1109/ACCESS.2025.3603226.

[2] U. Ali, S. Ullah, A. Basir, B. Kamal, L. Matekovits, and H. Yoo, "Design and SAR analysis of AMC-based fabric antenna for body-centric communication," IEEE Access, vol. 11, pp. 73894-73911, 2023, doi: 10.1109/ACCESS.2023.3295993.

[3] U. Ali, A. Basir, M. Zada, S. Ullah, B. Kamal, and H. Yoo, "Performance improvement of a dual-band textile antenna for on-body through artificial magnetic conductor," IEEE Access, vol. 11, pp. 72316-72331, 2023, doi: 10.1109/ACCESS.2023.3294412.

[4] Y. Thangavelu, B. Thangaraju, and R. Maheswar, "Design and SAR analysis of an AMC-integrated wearable cavity-backed SIW antenna," Micromachines, vol. 15, no. 12, Art. no. 1530, Dec. 2024, doi: 10.3390/mi15121530.

[5] J. Chu, C. Du, and H. Shu, "A high FBR low SAR and AMC-backed compact wearable antenna array for WBAN applications," Int. J. Microw. Wireless Technol., vol. 16, no. 9, pp. 1499–1509, Nov. 2024, doi: 10.1017/S1759078724001041.

[6] V. Rajavel and D. Ghoshal, "Enhancement of off-body communications with a low-SAR, high-gain multiband patch antenna designed with a quad-band artificial magnetic conductor," Int. J. Microw. Wireless Technol., vol. 16, no. 2, pp. 318–338, Mar. 2024, doi: 10.1017/S1759078723001174.

[7] V. Rajavel and D. Ghoshal, "Design of a low-SAR, high-gain multiband patch antenna with quad-band AMC for off-body communication applications," Appl. Phys. A, vol. 129, no. 8, Art. no. 576, Aug. 2023, doi: 10.1007/s00339-023-06856-y.

[8] C. Du, L.-R. Pei, J. Zhang, and C.-X. Shi, "A gain enhanced dual-band low SAR AMC-based MIMO antenna for WBAN and WLAN applications," Prog. Electromagn. Res. M, vol. 115, pp. 21–34, 2023, doi: 10.2528/PIERM22100201.

[9] T. Hussain, R. Fernández-García, and I. Gil, "Breathable artificial magnetic conductor with ground-grid structure for shielding wearable antenna sensors," Sens. Actuators A, Phys., vol. 391, Art. no. 116607, Sep. 2025, doi: 10.1016/j.sna.2025.116607.

[10] Y. A. Kamel, H. A. Mohamed, H. Elsadek, and H. El-Hennawy, "Flexible wearable antenna based on AMC with different materials for bio-telemetry applications," Prog. Electromagn. Res. M, vol. 127, pp. 1-10, 2024, doi: 10.2528/PIERM23121701.

[11] I. Aitbar, N. Shoaib, A. Alomainy, A. Quddious, S. Nikolaou, M. A. Imran, and Q. H. Abbasi, "AMC integrated multilayer wearable antenna for multiband WBAN applications," Comput. Mater. Continua, vol. 71, no. 2, pp. 3227-3241, 2022, doi: 10.32604/cmc.2022.023008.

[12] R. K. Merugumalli, N. A. Murugan, and S. R. Chalasani, "Design and optimization of a compact dual-band antenna using artificial neural networks for body area network applications," AEU-Int. J. Electron. Commun., vol. 200, Art. no. 155911, Oct. 2025, doi: 10.1016/j.aeue.2025.155911.

Uncorrected Proof

[13] R. Sandhya and A. Chandra, "A compact tree-shaped dual-band wearable antenna with enhanced far-field performance for WBAN applications," IEEE Access, vol. 13, pp. 152241–152252, 2025, doi: 10.1109/ACCESS.2025.3604551.

[14] U. Musa, A. Smida, M. S. Yahya, M. I. Waly, J. J. Tiang, N. K. Mallat, S. Muhammad, and A. Salisu, "Machine learning-optimized dual-band wearable antenna for real-time remote patient monitoring in biomedical IoT systems," Sci. Rep., vol. 15, Art. no. 30943, Aug. 2025, doi: 10.1038/s41598-025-15984-9.

[15] A. Salisu, M. A. Elwanis, I. Elfergani, U. Musa, A. Alfares, I. Gharbia, J. Rodriguez, C. H. See, and R. Abd-Alhameed, "Machine learning-optimized compact wearable frequency reconfigurable antenna for sub-6 GHz/mm-wave 5G integration," Sci. Rep., vol. 15, Art. no. 44912, Dec. 2025, doi: 10.1038/s41598-025-28971-x.

[16] M. S. Yahya, U. Musa, M. S. Zidan, S. Soeung, L. I. Izhar, Z. Zakaria, and A. J. A. Al-Gburi, "Machine learning-optimized compact dual-band medical syringe-inspired wearable antenna for efficient WBAN applications," Sci. Rep., vol. 15, Art. no. 43240, Dec. 2025, doi: 10.1038/s41598-025-27227-y.

[17] M. Bazgir, A. Sheikhi, and M. B. Dowlatshahi, "Resonance frequency prediction of dielectric antennas for liquid sensing via support vector regression," Sci. Rep., vol. 14, Art. no. 31410, Dec. 2024, doi: 10.1038/s41598-024-83069-0.

[18] A. K. Pandey and M. P. Singh, "Antenna optimization using machine learning algorithms and their applications: A review," J. Eng. Sci. Technol. Rev., vol. 17, no. 2, pp. 128–144, 2024, doi: 10.25103/jestr.172.14.

[19] R. Degachi and S. Ghendir, "Comparative analysis of machine learning models to predict rectangular patch antenna dimensions," J. Appl. Res. Technol., vol. 22, no. 6, pp. 781–790, Dec. 2024, doi: 10.22201/icat.24486736e.2024.22.6.2478.

[20] I. Merino-Fernandez, J. del Pino, and S. Khemchandani, "Design of rectangular patch antennas through machine learning," Sci. Rep., vol. 15, Art. no. 33605, Sep. 2025, doi: 10.1038/s41598-025-18939-2.

[21] H. T. P. Thao and T. V. Kien, "Hybrid machine learning and Gaussian process for antenna parameter estimation," Sci. Rep., vol. 16, Art. no. 6076, Jan. 2026, doi: 10.1038/s41598-026-35564-9.

[22] M. A. Haque, M. A. Rahman, S. S. Al-Bawri, Z. Yusoff, A. H. Sharker, W. M. Abdulkawi, D. Saha, L. C. Paul, and M. A. Zakariya, "Machine learning-based technique for gain and resonance prediction of mid band 5G Yagi antenna," Sci. Rep., vol. 13, Art. no. 12590, Aug. 2023, doi: 10.1038/s41598-023-39730-1.

[23] C. Wang, Y. Zhang, S. Gao, and W. Liu, "Design of sparse antenna arrays using the physics-aware generative adversarial network," IEEE Trans. Antennas Propag., vol. 73, no. 9, pp. 6311–6325, Sep. 2025, doi: 10.1109/TAP.2025.3570528.

[24] Y. Saifullah, N. Wu, H. Wang, B. Zheng, C. Qian, and H. Chen, "Deep learning in metasurfaces: From automated design to adaptive metadevices," Adv. Photon., vol. 7, no. 3, Art. no. 034005, 2025, doi: 10.1117/1.AP.7.3.034005.

[25] M. K. Shereen, X. Liu, X. Wu, S. U. Din, A. Naseem, S. Niazi, and M. I. Khattak, "Innovations in metamaterial and metasurface antenna design: The role of deep learning," Mater. Today Electron., vol. 13, Art. no. 100162, 2025, doi: 10.1016/j.mtelec.2025.100162.

[26] S. Dodge, N. Fontana, M. E. Mognaschi, E. Canicattì, and S. Barmada, "A deep learning based prediction of specific absorption rate hot-spots induced by broadband electromagnetic devices," IET Sci. Meas. Technol., vol. 19, no. 1, Art. no. e70009, 2025, doi: 10.1049/smt2.70009.

[27] Determining the Peak Spatial-Average Specific Absorption Rate (SAR) in the Human Body From Wireless Communications Devices, 30 MHz to 6 GHz—Part 1: General Requirements for Using the Finite Difference Time-Domain (FDTD) Method for SAR Calculations, IEC/IEEE 62704-1:2017, Oct. 2017.

[28] Radiofrequency Radiation Exposure Limits, 47 C.F.R. § 1.1310, Federal Communications Commission.

[29] ICNIRP, "Guidelines for limiting exposure to electromagnetic fields (100 kHz to 300 GHz)," Health Phys., vol. 118, no. 5, pp. 483–524, 2020, doi: 10.1097/HP.0000000000001210.

[30] 29. S. Ahmad, K. N. Paracha, Y. A. Sheikh, A. Ghaffar, A. D. Butt, M. Alibakhshikenari, P. J. Soh, S. Khan, and F. Falcone, “A metasurface-based single-layered compact AMC-backed dual-band antenna for off-body IoT devices,” IEEE Access, vol. 9, pp. 159598–159613, 2021.

Uncorrected Proof

AUT Journal of Electrical Engineering
10.22060/EEJ.2026.26568.6160

Uncorrected Proof